Structure, magnetism, and spin-phonon coupling in heteroepitaxial La₂CoMnO₆/Al₂O₃(0001) films

Ch. Meyer,[1] V. Roddatis,[2] P. Ksoll,[1] B. Damaschke,[1] and V. Moshnyaga[1]

[1]*Physikalisches Institut, Georg-August-Universität Göttingen, Friedrich-Hund-Platz 1, 37077 Göttingen, Germany*
[2]*Institut für Materialphysik, Georg-August-Universität Göttingen, Friedrich-Hund-Platz 1, 37077 Göttingen, Germany*

Double perovskite La₂CoMnO₆ (LCMO) thin films with the monoclinic $P2_1/n$ structure were grown on hexagonal *c*-cut sapphire substrates by metalorganic aerosol deposition technique. Epitaxial growth of LCMO(021)/Al₂O₃(0001) due to an almost perfect in-plane lattice matching between LCMO and Al₂O₃ was evidenced by x-ray diffraction and transmission electron microscopy. A high degree of rock-salt-type Co/Mn ordering was directly visualized by means of high resolution transmission electron microscopy. The *B*-site ordering, influenced by the film growth rate and optimized by small compressive epitaxial strain, results in perfect magnetic properties and strong spin-phonon coupling, both necessary requisites for multiferroic performance.

I. INTRODUCTION

The La₂CoMnO₆ (LCMO) with the monoclinic $P2_1/n$ structure [1,2] from the $A_2BB'O_6$ family of double perovskites is a promising material system for spintronic applications due to the presence of ferromagnetic ordering, magnetodielectric coupling, and multiferroic behavior [2–6]. This material can be also used as a model system to study the coupling between spin, charge, and lattice degrees of freedom, since electromagnetic properties of LCMO depend strongly on the degree of *B*-site ordering, controlled as well by the size- and valence-mismatch of *B* cations [2,7–10].

The *B*-site ordering in LCMO is of rock-salt type with Co^{2+} and Mn^{4+} cations alternatingly occupying the *B* sites in the perovskite structure ABO_3 [8,9,11]. According to the second rule of Goodenough-Kanamori-Anderson, a superexchange interaction between the high-spin $Co^{2+}(3d7, t_2g^5e_g^2, S = 3/2)$ and $Mn^{4+}(3d3, t_2g^3e_g^0, S = 3/2)$ ions results in a ferromagnetic (FM) state with Curie temperature, $T_C \sim 230$ K, and theoretical saturation magnetization, $M_s = 6 \mu_B$/f.u., for a perfect ordering [5,9]. Deviations from the ideal Co/Mn ordering, caused by point defects or multiple nucleation, result in Co^{2+}-O-Co^{2+} and Mn^{4+}-O-Mn^{4+} antiphase boundaries (APB) of the antiferromagnetic (AFM) type. They act as domain walls between the FM domains, within which a short-range Co^{2+}/Mn^{4+} ordering exists [6,10]. The AFM coupling of the FM domains causes a lowered remanent magnetization, which still can be transformed into a fully aligned one-domain FM state in a strong applied magnetic field, $B \sim 5$ T [10].

In contrast, a fully disordered LCMO (chemical formula LaCo₀.₅Mn₀.₅O₃) crystallizes in an orthorhombic P_{bnm} structure with randomly distributed $Co^{3+}(3d6, t_2g^5e_g^1, S = 1)$ and $Mn^{3+}(3d4, t_2g^3e_g^1, S = 2)$ ions. These ionic states result from an e_g-electron transfer from Co^{2+} to Mn^{4+} ions, stabilized by the local Jahn-Teller distortions and/or oxygen deficiency [6,11]. The vibronic super-exchange interaction between Co^{3+} and Mn^{3+} leads to a lowered $T_C \sim 135$ K and substantially reduced $M_S = 3.5$–$4.5 \mu_B$/f.u. [6,10,11]. Thus,

the saturation magnetization can be viewed as an indirect measure of the short-range *B*-site ordering [6,8,10] and the density of APBs [10].

A long-range *B*-site ordering can be evidenced by x-ray (XRD) and electron diffraction. Double perovskites with a rock-salt *B*-site ordering can be viewed as an infinite superlattice along the pseudo-cubic [111] direction with alternating LaMnO₃ and LaCoO₃ perovskite layers. The doubling of an effective lattice parameter generates superlattice reflections in the XRD pattern [6,8,8,13–15]. Their intensity depends on the difference between the atomic form factors of the *B* cations [9,12,13] as well as on the degree of *B*-site ordering. A similar effect can also be caused by an octahedral tilting as well as due to the displacements of *A*-site cations and anions [9,12,13]. Hence, a careful analysis in combination with magnetization data and chemical mapping by electron-energy-loss spectroscopy (EELS) with scanning transmission electron microscopy (STEM) is necessary to confirm the *B*-site ordering.

In addition, Raman spectroscopy was shown to be a powerful technique to characterize *B*-site ordering since it results in a monoclinic $P2_1/n$ structure. In contrast, the *B*-site disordered modification yields an orthorhombic P_{bnm} structure, which can be easily distinguished due to different symmetry and selection rules of the corresponding Raman modes [3,16]. Polarized Raman spectroscopy was studied in single crystals [18–20] and thin films [3,16,17,20–22] of LCMO and similar double perovskites [18,19,23–26]. Finally, the effect of the *B*-site ordering on the spin-phonon coupling as well as on structural transformations [16–21] can be elucidated from the temperature behavior of Raman spectra, which, however, was only measured for the LCMO films grown on STO(100) substrate [16,17]. Moreover, no quantitative estimation of spin-phonon coupling in LCMO films as well as of its relation to the short/long-range *B*-site ordering was done up to now to the best of our knowledge.

Usually, epitaxial LCMO films have been grown by pulsed laser deposition (PLD) and by radio-frequency (rf) sputtering on single crystalline perovskite substrates, i.e., SrTiO₃ (STO),

LaAlO$_3$ (LAO) or (La$_{0.3}$Sr$_{0.7}$)(Al$_{0.65}$Ta$_{0.35}$)O$_3$ (LSAT), with a large lattice misfit, $\varepsilon = 100\% * (a_{film} - a_{sub})/a_{film} = 1 - 3\%$ [11,16–18,20,27–31]. As a rule, the (100)-oriented substrates were used so that the *B*-site ordering could be estimated only indirectly from the magnetization data [4,5,10,27,28] or Raman spectroscopy [16,17,20]. In contrast, there were only few reports on the LCMO/STO(111) films, in which the *B*-site ordering obtained from XRD was compared with EELS and STEM [10,27]. Note that the influence of epitaxy strain on the spin-phonon coupling has not been reported up to now, to the best of our knowledge.

Here we report on the structure, magnetic, and phonon properties of LCMO thin films, heteroepitaxially grown on hexagonal Al$_2$O$_3$ (0001) substrates. The goal of our study was, on one hand, to demonstrate a way to grow a high quality LCMO films on a new substrate, i.e., sapphire, as well as, on the other hand, to study the interplay between stress and short/long-range *B*-site ordering (structurally and chemically). A short- and long-range *B*-site ordering was determined quantitatively and qualitatively by magnetization, XRD, STEM, EELS, as well as by the anomalous mode softening due to spin-phonon-coupling in the FM phase.

II. EXPERIMENTAL DETAILS

Double perovskite LCMO epitaxial thin films with thicknesses $d = 100$ nm were grown on *c*-axis-oriented Al$_2$O$_3$(0001) substrates by a metalorganic aerosol deposition (MAD) technique using a solution of acetylacetonates of La, Co and Mn in dimethylformamide under ambient oxygen partial pressure ($pO_2 \sim 0.21$ mbar). For the growth the substrate was heated to a substrate temperature of $T \sim 1000\,°C$ with a heating rate before and a cooling rate of $\sim 50\,K/min$ after the deposition process as well [10,32–34]. Two films, grown with different growth rates, $r = 6$ and 12 nm/min, and showing a contrast behavior, are called in the following as "ordered" (O) and "partially disordered" (PD), respectively. X-ray reflection (XRR) and XRD (Cu-K$_\alpha$ radiation, Bruker AXS D8 Advance) were used to characterize the thickness of the films and their crystalline quality. The temperature- and field-dependent magnetization was measured by using of a superconducting quantum interference device (SQUID) magnetometer (MPMS 3, Quantum Design) at temperatures, $T = 5–300$ K, and applied magnetic fields, $B = 0–5$ T. Raman spectra were recorded by a LabRAM HR Evolution (HORIBA Jobin Yvon) spectrometer in the backscattered top-illumination geometry. Raman measurements in the temperature range, $T = 80–620$ K, were performed by using a Linkam THMS350EV thermal vacuum stage. The sample illumination and the collection of the backscattered light was done by using a 50 × magnification long-working-distance objective (Olympus, NA = 0.5). The excitation was carried out by a second harmonic generation of a linear polarized Nd:YAG laser ($\lambda = 532$ nm, Laser Quantum torus 532) with incident power 2 mW at the film surface and spot size $\sim 1\,\mu m^2$. Polarized Raman spectra were recorded for the film orientation $x \parallel [11\bar{2}]$ parallel to the incident laser polarization, $y \parallel [\bar{1}10]$ perpendicular to it and $z \parallel [021]$ in the direction of light propagation normal to the film surface. The polarization of scattered light is filtered by an analyzer with two configurations (x and y) in front

of the detector, so that xx implies parallel scattering with the analyzer aligned parallel to the incident laser polarization, whereas xy represents cross-scattering polarization with the analyzer perpendicular to the incident laser polarization. Local structure of LCMO films was studied by transmission electron microscopy (TEM). Low magnification and high resolution (HR) annular bright field (ABF) and high-angle annular dark-field (HAADF) images were collected with an FEI Titan 80–300 G2 environmental transmission electron microscope (ETEM), operated at an acceleration voltage of 300 kV. The microscope is equipped with a Gatan Image Filter (GIF) Quantum 965ER for chemical element mapping using (EELS. TEM lamellas were prepared by Focused Ion Beam (FIB) lift-out technique using an FEI Nova NanoLab 600 instrument.

III. RESULTS AND DISCUSSION

A cross-section low magnification high-angle annular dark-field (HAADF) image of the LCMO O film is shown in Fig. 1(a). One can see a well-defined and flat film/substrate interface as well as dark and bright domains with a typical size of 100–200 nm. Quantitative analysis of the chemical composition within domains with different contrast shows a perfect agreement with the desired stoichiometry, i.e., Co/Mn = 50/50 ± 2%, indicating that the observed contrast has not a chemical origin. A high resolution HAADF STEM image [see Fig. 1(b)], taken over the region consisting of dark (1) and bright (2) domains, shows that they have different crystallographic orientation: [021] and [201], respectively. The domains projected along [100] axis of the film (in this case [021]$_{LCMO} \parallel [0001]_{Al_2O_3}$) appear darker in the HAADF image, while the domains projected along [010] axis ([201]$_{LCMO} \parallel [0001]_{Al_2O_3}$) look brighter, because of the diffraction component at the used imaging conditions. The fast Fourier transforms (FFTs) of selected areas (1 and 2) demonstrate different patterns, which both are in a good agreement with the simulated diffraction patterns of the monoclinic $P2_1/n$ space group of the LCMO [35]. The atomic models of this structure, projected along [100] and [010] axes, are shown in Fig. S1(a) and S1(b), respectively [36]. Based on the analysis of experimental and calculated diffraction patterns we conclude that the LCMO O film belongs to the monoclinic structure, which is characteristic for double perovskites and for the *B*-site ordering as well. It is worth noting that the LCMO film matches perfectly the Al$_2$O$_3$ substrate as it can be seen in Fig. 1(c). The slightly changed contrast indicates a possible reconstruction at the interface. Finally, atomically resolved EELS maps, constructed by using the Co-$L_{2,3}$ and Mn-$L_{2,3}$ edges, evidence a robust *B*-site ordering in the O film as shown in Fig. 1(d). Similar maps were observed within different domains of the film.

The enlarged HR-STEM image of a domain boundary (DB), highlighted by semitransparent area, between [100]- and [010]-projected domains is shown in Fig. 2(a). A careful study of the images from many DBs did not reveal any structural defects (dislocations, secondary phases, etc.). Moreover, the chemical mapping of Mn and Co distribution in Fig. 2(b) shows that the Co/Mn ordering is not broken across the DB. What we observed is only a slight misorientation between
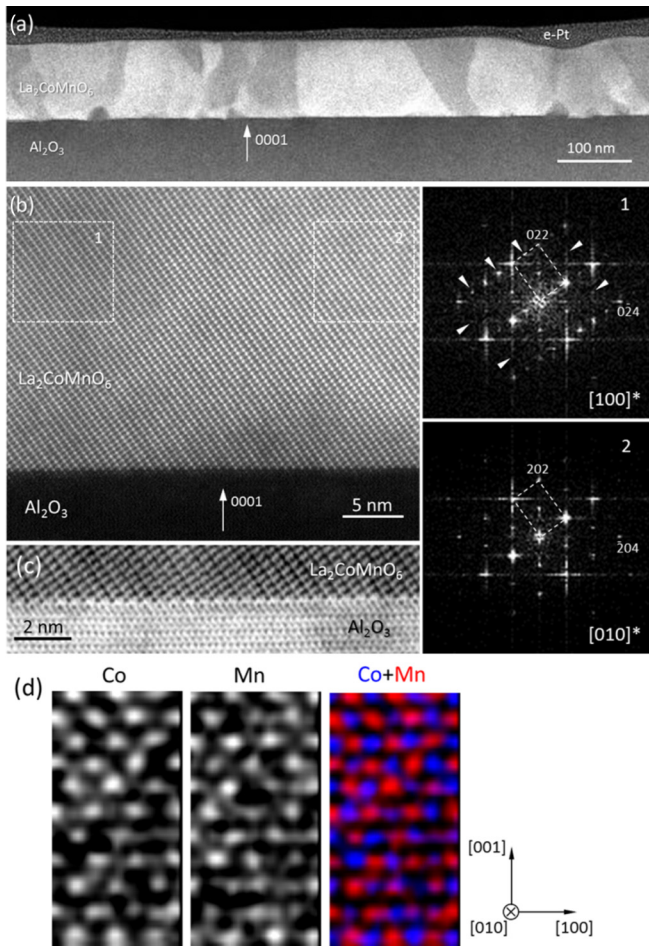
FIG. 1. (a) Low-magnification HAADF STEM image of an LCMO film grown on Al_2O_3(0001) substrate with a rate 6 nm/min. (b) HR STEM image of LCMO film with FFT patterns from areas marked as "1" and "2". Rows of spots with a doubled periodicity marked with the white arrowheads in the FFT from the area "1" indicate the monoclinic $P2_1/n$ space group. (c) HR ABF image of a defect-free LCMO/Al_2O_3 interface. (d) EELS map of Co, Mn, and Co+Mn atoms of a representative section of the film along the [010] axis demonstrates the rock-salt ordering of Co and Mn atoms.
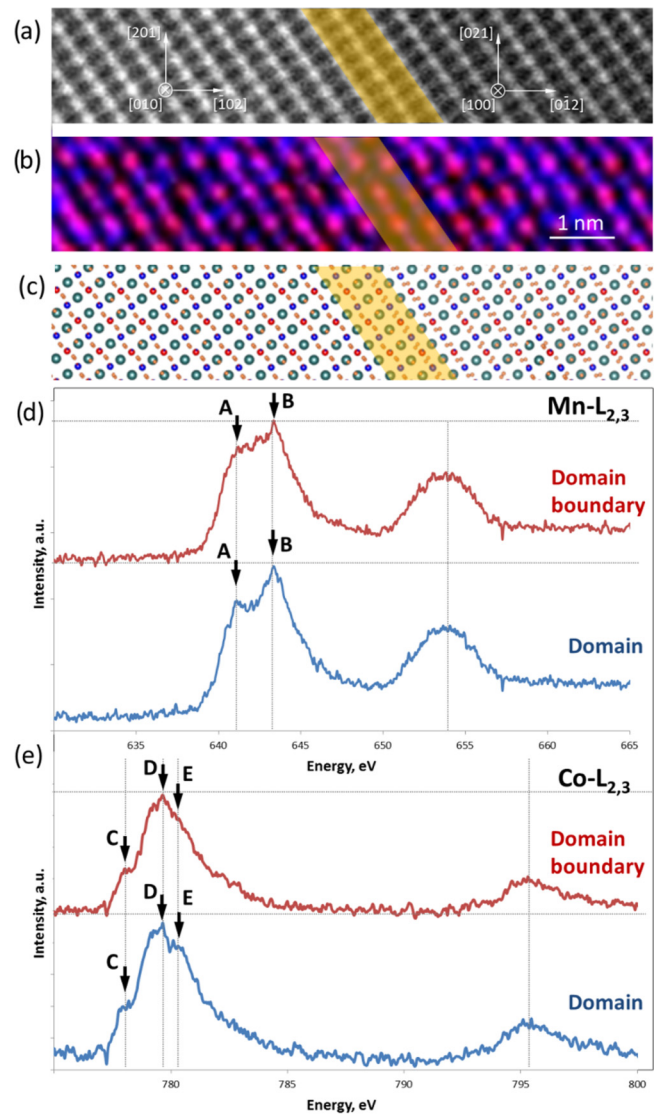

FIG. 2. Microstructure of the LCMO O film: (a) HR-STEM image; (b) the corresponding EELS mapping, showing Co/Mn ordering within crystallographic domains and domain boundary (DB), and (c) unrelaxed atomic model of DB. The high energy resolved spectra of the Co and Mn cations within the domains and at the DB: (d) for Mn-$L_{2,3}$, and (e) for Co-$L_{2,3}$ edges. The features marked with the black arrows and denoted as A = 641 eV and B = 643 eV for Mn-$L_{2,3}$ edge and C = 778 eV, D = 779.6 eV, E = 780.3 eV for Co-$L_{2,3}$ indicate the corresponding spectral differences between domains and DBs.

the [201] and [012] directions of two adjacent structural domains, which does not exceed 0.3°. The reconstructed atomic model of the unrelaxed DB between the [021]- and [201]-oriented and B-site ordered domains in Fig. 2(c) shows that two domains can form a defect-free DB simply sharing common La atoms. In order to assess the valence of Mn and Co ions the experimental core loss spectra were taken from both bulk and DB areas of the sample for the Mn-$L_{2,3}$ and for the Co-$L_{2,3}$ edges, collected under similar conditions. The high-energy resolved spectra show the characteristic features in the Mn-L_2 edge, denoted as "A" (641 eV) and "B" (643 eV) in Fig. 2(d), and Co-L_2 edge, denoted as "C" (778 eV), "D" (779.6 eV) and "E" (780.3 eV) in Fig. 2(e). The positions of the Mn-L_3 and Co-L_3 edges remain almost unchanged. The detailed analysis of oxidation states of Co and Mn ions in the LCMO/STO(111) double perovskite films, based on the reference spectra of different Co and Mn oxides, was reported recently by Egoavil *et al.* [10]. A comparison with Ref. [10]

shows that the clearly visible A and B features (peaks) at the Mn-L_2 edge evidence the presence of Mn^{4+} ions within the domain, while a smoothed shoulder at A indicates the presence of Mn^{3+} ions within the DB. Similarly, the features C, D, and E seen in the Co-L_2 edge within the crystallographic domain indicate the presence of Co^{2+} ions there. In contrast, the peak E is not visible in the spectra collected from the DB area, indicating the presence of Co^{3+} within DBs. Thus, the EELS spectra collected from the DB areas reveal a moderate, but measurable changes of the spectral shape of both Co and Mn-$L_{2,3}$ edges with respect to the spectra taken within the
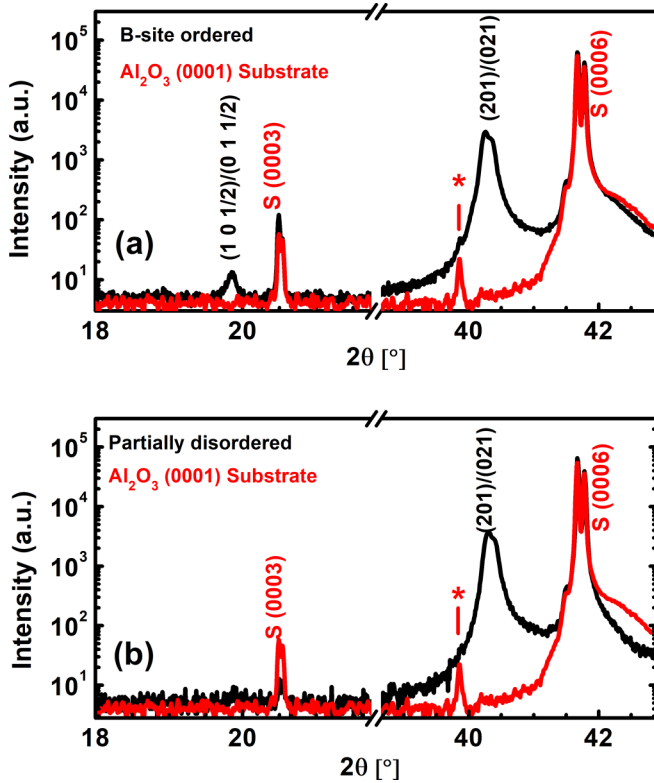
FIG. 3. The XRD pattern of the two LCMO/Al$_2$O$_3$ (0001) films with thicknesses $d = 100$ nm, grown with a growth rate of 6 nm/min (a) and 12 nm/min (b); the blank substrates are shown in red. The film reflections are indicated in the monoclinic $P2_1/n$ notation, whereas the S symbolizes substrate-related reflections. The star marks the not totally filtered out Cu-K$_\beta$ radiation from the x-ray anode.

domains. The EELS spectra of domains reproduce qualitatively the main spectral features of the B-site ordering, i.e., the dominance of Co^{2+} and Mn^{4+} ionic states, in close agreement with the previous study on the LCMO/STO(111) film [10]. In contrast, the spectral shapes of Co and Mn edges in the spectra collected from DBs indicate the increased amount of Mn^{3+} and Co^{3+} ions within the DBs. This points out the relaxation of the orientation misfit of 0.3° between the domains by means of changing the lengths of atomic bonds, yielding the Jahn-Teller distortion with formation of Co^{3+}/Mn^{3+} and accompanying changes in the oxygen sublattice. Thus, the observed DBs manifest themselves as electronic defects of the B-site ordering, which likely can be influenced by the choice of substrate and growth conditions. However, considering the small amount of such defects, ∼2–4%, they seem to be not playing a dominant role in the magnetism of LCMO.

In Fig. 3(a) and 3(b) the XRD patterns are shown for O and PD films, respectively. One can clearly see the out-of-plane epitaxy with the (021)/(201) plane of LCMO (we cannot resolve between them with our XRD setup) aligned parallel to the (0001) plane of sapphire. The calculated pseudocubic lattice parameter, $c_O = 0.3878$ nm for and $c_{pd} = 0.3874$ nm are close to the corresponding bulk value of LCMO, $c_{bulk} = c/\sqrt{2} = 0.3887$ nm [37]. Moreover, the (α_1-α_2) splitting of the (021) peak of LCMO evidences a high crystalline quality

of films in agreement with TEM observations. The obtained heteroepitaxial growth of LCMO on sapphire can be interpreted by simple geometric considerations under assumption of the pseudocubic structure of LCMO. Because of a hexagonal symmetry of the (111) pseudocubic (pc) interface plane, the growth mode of LCMO on sapphire is similar to the films with rock-salt structure, such as MgO(111) on the Al$_2$O$_3$(0001) substrates [38,39] and, in another way, of a hexagonal ZnO(0001) on a cubic STO(111) [40,41]. In the case of LCMO$_{pc}$(111)/Al$_2$O$_3$(0001) the effective in-plane lattice constant within the LCMO(111) is $a_{pc}/\sqrt{2}$, that is the half of the diagonal of the pseudocubic cell. Hence, a reduction of the lattice mismatch between Al$_2$O$_3$(0001) and LCMO$_{pc}$(111) is accomplished by 30° in plane rotation of LCMO relative to the substrate, since the apothem of the in-plane hexagonal structure of the Al$_2$O$_3$ is approximately identical to three times the effective in-plane lattice constant of LCMO. This results in the epitaxy relation $\sqrt{2}a_{sapphire} = \sqrt{3}a_{pc}$. With $a_{sapphire} = 0.4758$ nm [42] one can calculate that an ideal (misfit-free) cubic material should have an effective in-plane lattice constant, $a_{eff} = 0.3885$ nm. Considering $a_{pc} = 0.3887$ Å of the bulk LCMO [37], the theoretical in-plane lattice mismatch between Al$_2$O$_3$ and LCMO is only 0.05%. As the pseudocubic out-of-plane lattice constant of our LCMO films is slightly reduced compared to the bulk LCMO, a small compressive strain in the out-of-plane direction of −0.18% and −0.28% for the O and PD film, respectively, could be assumed.

Besides the strong (021)/(201) peak in Fig. 3(a) one can also see a superlattice (0 1 $^1/_2$)/(10$^1/_2$) peak, signaling the presence of the B-site ordering in the O film. As this peak is missing in Fig. 3(b), the B-site ordering seems to be reduced in the PD film. The degree of B-site ordering with the rock-salt structure in $A_2BB'O_6$-type double perovskites can be estimated from the XRD intensity ratio, $S = I(^1/_2{}^1/_2{}^1/_2)/I(111)$, in the pseudocubic notation [10,12]. The evaluated value, $S \sim 7 \times 10^{-3}$, for the O film is smaller than $S = 10^{-2}$, simulated for a perfectly B-site ordered LCMO [10]. However, the S values have to be taken with a caution as other factors can strongly influence it. First, the intensity of the superlattice peak scales with the difference in the atomic form factors of the B-site cations [12,13]. For Co^{2+} and Mn^{4+} with very similar atomic form factors the $I(^1/_2{}^1/_2{}^1/_2)$ is strongly reduced and differs not too much from the background [27]. Second, the presence of APBs can lead to the underestimation of the B-site ordering from the XRD measurements due to a possible out-of-phase orientation of ordered domains with different or irregular shape. Third, a displacement of the A-site cations and the oxygen in the structure can mimic the B-site ordered double perovskite supercell even if the B-site cations are randomly distributed [10,12,13,27]. Hence, the observation of a superstructure in the XRD pattern alone is generally not a sufficient proof for the chemical order in the double perovskites.

Magnetization as a function of temperature for the O and PD film is shown in Fig. 4. The films exhibit a ferro/paramagnetic transition with Curie temperature, $T_{C-O} = 228$ K and $T_{C-PD} = 226$ K, calculated from the minimum of the temperature coefficient of magnetization,

FIG. 5. Magnetization loops, $M(H)$, for B-site ordered (black) and partially disordered (red) LCMO/Al$_2$O$_3$ (0001) films, measured at $T = 5$ K.
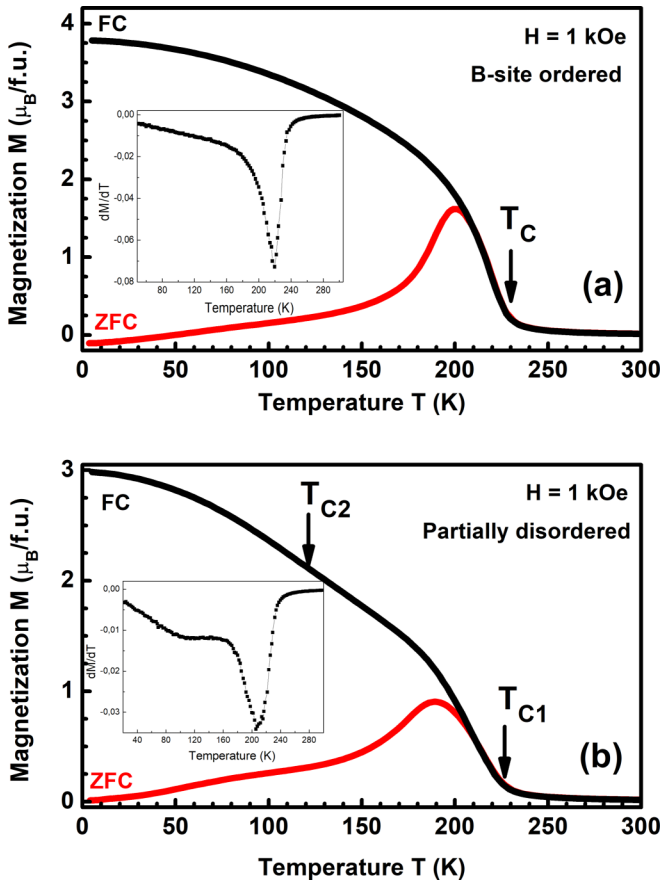

FIG. 4. The field-cooled (FC) and zero-field-cooled (ZFC) temperature dependences of magnetization, $M(T)$, of the B-site ordered (a) and partially B-site disordered LCMO/Al$_2$O$_3$ (0001) films, measured in an external magnetic field of $H = 1$ K. The dM/dT curves shown in the insets, illustrate a single (a) and double transition (b) in B-site ordered and partially disordered films, respectively.

TCM $= (1/M)(dM/dT)$. For the PD film a second ferromagnetic transition at $T_{C2-PD} = 110$ K can be also seen in Fig. 4(b). This behavior is in agreement with previous results, demonstrating a single $T_C \sim 230$ K due to an FM Co^{2+}-O-Mn^{4+} superexchange in the B-site ordered samples and a second transition at $T_C \sim 80$–130 K due to the weaker Co^{3+}-O-Mn^{3+} vibronic superexchange interaction in the B-site disordered samples [6,10,11,27,43]. Moreover, a strong difference between the field-cooled (FC) and zero-field-cooled (ZFC) $M(T)$ curves can be seen in Fig. 4, which is usually assigned to a cluster-glass-like behavior with a cusp in magnetization near T_C and zero net moment for $T \ll T_C$ due to an FM/AFM competition [10,11,35,44,45]. However, considering the observed crystallographic domain structure and the robust Co/Mn ordering within domains (see Figs. 1 and 2) the suppression of ZFC magnetic moment could be explained by the strong magnetocrystalline anisotropy in LCMO, the easy axis of which lies in different directions in differently oriented crystallographic domains.

In Fig. 5 we present $M(H)$ curves for both films, measured at $T = 5$ K. The O film shows the saturation magnetization, $M_{S\text{-}O} = 5.91 \mu_B/$f.u., which is close to the theoretical value, $M_{th} = 6 \mu_B/$f.u. [6] The estimated degree of short-
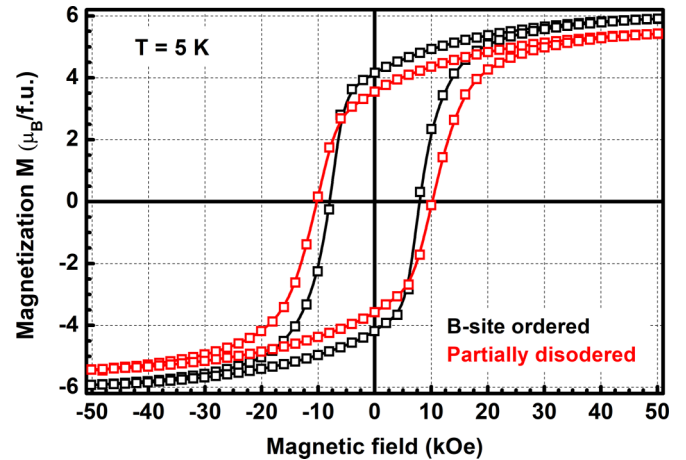
range B-site ordering in the O film is thus $M_{S\text{-}O}/M_{th} = 98\%$. For the PD film with significantly smaller, $M_{S-PD} = 5.43 \mu_B/$f.u., the estimated degree of short-range ordering reduces to $M_{S\text{-}PD}/M_{th} \sim 90\%$, being in agreement with a partial disorder observed in the XRD. Moreover, the coercive field, H_c, and the remanent magnetization, M_R, are also different for the O and PD film. Indeed, the O film shows $H_{c\text{-}O} = 7.7$ kOe and $M_{R\text{-}O} = 4.2 \mu_B/$f.u., whereas the PD film displays a higher coercitvity, $H_{c\text{-}PD} = 10.2$ kOe, and a lowered remanence, $M_{R\text{-}PD} = 3.6 \mu_B/$f.u. According to a magnetic model of LCMO [10] the larger coercive field and the lowered remanent magnetization infer a higher density of defects and a smaller size of FM domains. Thus, direct evidence for a different degree of B-site ordering for LCMO/Al$_2$O$_3$(0001) films (O and PD) is maintained from the $M(H)$ measurements. In this context a reduced M_S of the PD-film, compared to the O-film, is attributed to a higher amount of AFM-ordered spins at point antisite cations [6]. The APBs will completely flip to an FM alignment in a strong magnetic field, $H \sim 50$ kOe, and will not contribute for this reason to the lowering of M_S [6,10]. Note, that the estimated from the saturation magnetization degree of B-site ordering of 98% relates only to the short-range ordering. However, taking into account a robustness of Co/Mn ordering, directly visualized in EELS maps (see Figs. 1 and 2) in different domains of the TEM sample (O-film) as well as a small amount of defects (DBs), one can suggest a high degree of the long-range B-site ordering. In earlier reports on LCMO films one can also find high values of $M_S = 5.8 \mu_B/$f.u., which is equivalent to $\sim$97% of short-range ordering (see Ref. [4]), but no data on the long-range ordering were provided.

In Fig. 6 the polarization dependences of room temperature Raman spectra are shown for the parallel xx scattering and the crossed scattering. The important Raman features are (1) a strong sharp mode (also called breathing mode) at 646 cm^{-1} and 644 cm^{-1} for the O and PD film, respectively, and (2) a broader and less intensive band at 498 and 497 cm^{-1} for the O and PD film, respectively. Theoretical lattice dynamics calculations [16] confirm that the sharp mode at $\sim$646 cm^{-1}

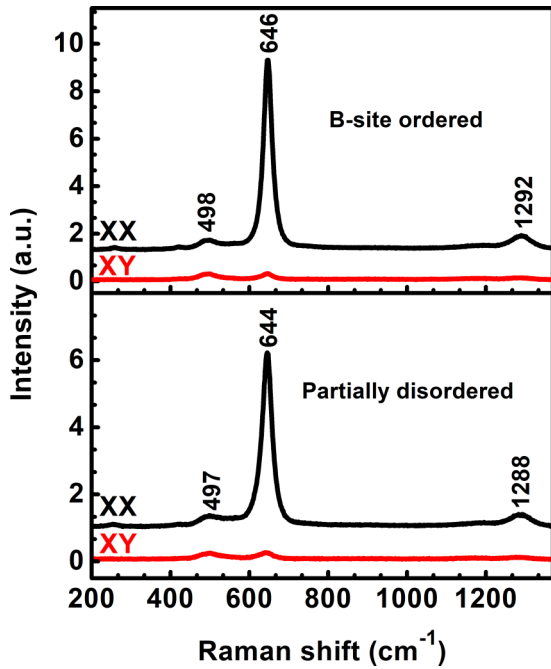FIG. 6. Polarized Raman spectra of LCMO/Al$_2$O$_3$ (0001) films in the parallel (xx scattering) and crossed (xy scattering) polarization combination, measured at $T = 300$ K.

originates from a symmetric stretching of the (Co/Mn)O$_6$ octahedra, whereas the band at around 498 cm^{-1} describes a mixed type vibration of antisymmetric stretching and bending. Additionally, the modes at ∼1292 and ∼1288 cm^{-1} for the O and PD-film, respectively, represent the second-order overtones of the breathing mode [22]. For the B-site ordered LCMO with a monoclinic $P2_1/n$ structure the breathing mode obeys the A_g symmetry and, thus, should be allowed in the parallel xx scattering and forbidden in the crossed xy scattering. For the B-site disordered structure the breathing mode displays B_{1g} symmetry with the opposite Raman selection rules [16,17,22]. One can see in Fig. 6(a), that both LCMO films show an almost identical polarization behavior: a strong breathing mode is seen in the parallel xx scattering and it is suppressed in the crossed xy scattering. Hence the ordered and partially disordered films can be assigned to a monoclinic $P2_1/n$ structure.

The temperature dependences of the position, $\omega(T)$, and the width, $\Gamma(T)$, of the A_g breathing mode for $T = 80$–600 K of the O- and PD-film are shown in Figs. 7(a) and 7(b). These dependences originate from the anharmonic corrections in the potential energy of the (Mn/Co)O$_6$ vibration. We fitted the measured temperature behavior of the A_g mode by an anharmonic model by considering cubic anharmonic constants in the potential energy [46–48]. The anharmonic model fits nicely the position, $\omega(T)$, for $T_C < T < 500$ K, and the linewidth, $\Gamma(T)$, of the A_g breathing mode. The two distinct deviations from the anharmonic behavior in $\omega(T)$ are (1) a phonon hardening for $T > 500$ K, which can be assigned to a structural phase transition at $T_{MR} = 580$ K (O film) and $T_{MR} = 560$ K (PD film) according to the earlier neutron [1] and recent Raman [20,21] measurements on bulk and thin films of LCMO, and (2) a softening of the breathing
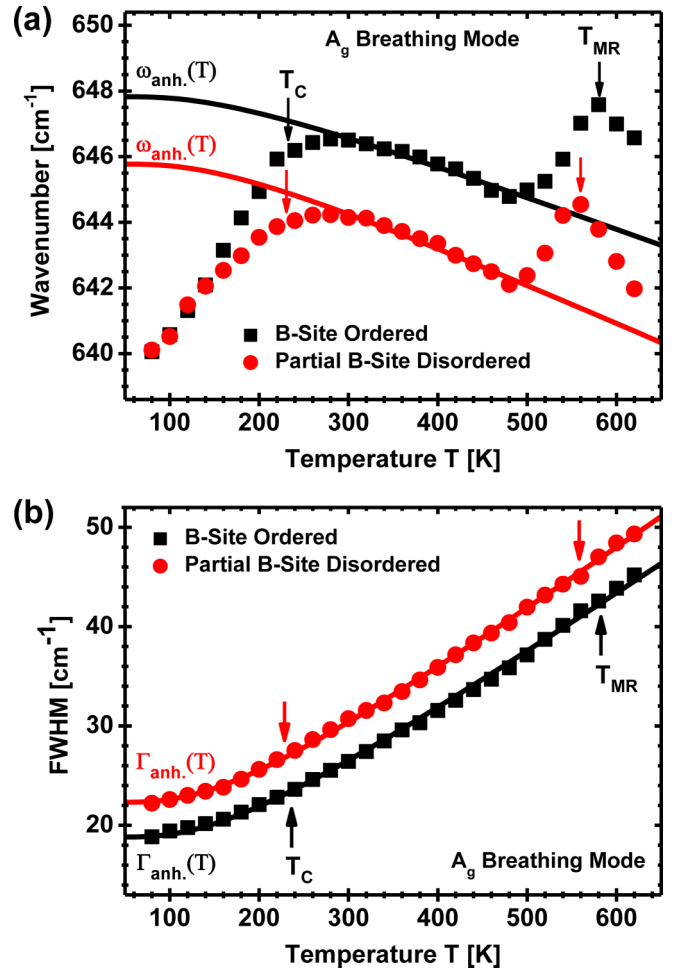

FIG. 7. Temperature dependences of the position (a) and of the linewidth (b) of breathing A_g mode for LCMO/Al$_2$O$_3$ (0001) films. Solid lines denote the temperature evolution of the anharmonic three-phonon model.

mode in the FM state for $T < T_C$. The anomalous softening of the A_g breathing mode for $T < T_C$ originates from a phonon renormalization due to an FM ordering and results in a coupling between the spin and lattice (phonon) degrees of freedom as was also shown for the FM manganites [49,50] and cobaltates [50]. Considering the nearest-neighbor spin-spin interaction, the phonon renormalization $\Delta\omega(T) = \omega(T) - \omega_{anh}(T)$ is proportional to the spin-spin correlation function $\langle S_i \cdot S_j \rangle$ between the spins at the ith and j^{th} sites, which scales as well with the normalized magnetization $M^2(T)/M_{max}^2$ in a molecular mean-field approximation [16,49–51]. Considering four nearest neighbors for each B-site cation in LCMO one gets for $\Delta\omega(T)$ [49–51]

$$\Delta\omega(T) = \omega(T) - \omega_{anh}(T) \approx -\lambda\langle S_i \cdot S_j \rangle \approx -4\lambda\frac{M^2(T)}{M_{max}^2}. \quad (1)$$

The spin-phonon coupling is quantified by the spin-phonon coupling strength, λ, whereas M_{max} is the saturation magnetization approximated to $T = 0$ K.
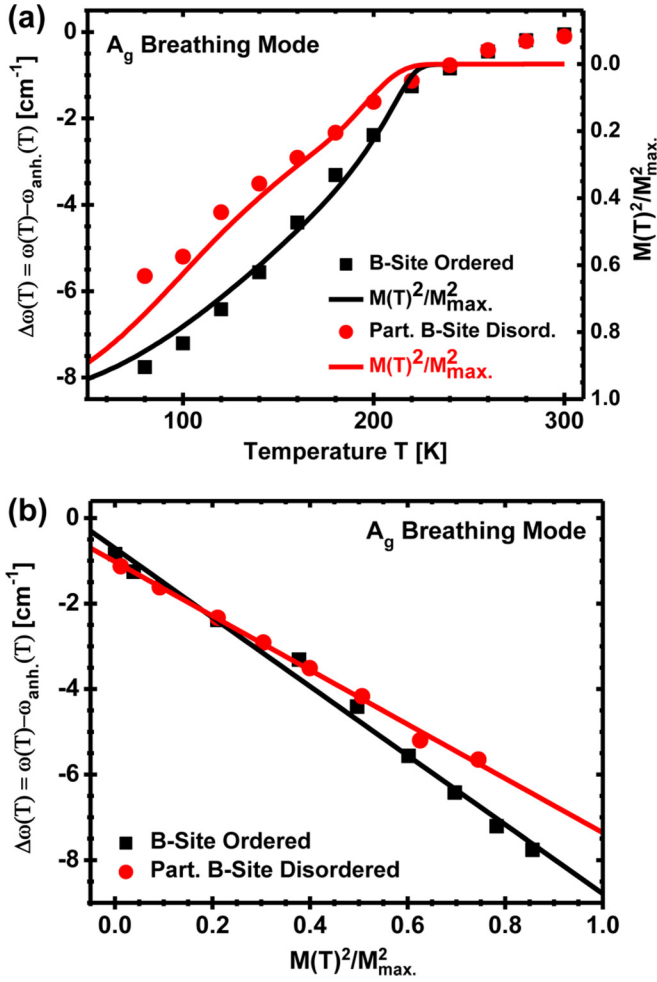
FIG. 8. A comparison of the deviation of the A_g breathing mode, $\Delta\omega(T)$, from the anharmonic three-phonon model and the normalized $M^2(T)/M^2_{max}$ for LCMO/Al$_2$O$_3$ (0001) films with different degree of B-site ordering (a) and the resulting linear dependence of $\Delta\omega(T)$ on the squared relative magnetization, $M^2(T)/M^2_{max}$, for both films (b).

As one can see in Fig. 8(a), the experimentally measured $\Delta\omega(T) = \omega(T) - \omega_{anh}(T)$ is nicely fitted by the normalized magnetization, $M^2(T)/M^2_{max.}$, thus, verifying that anomalous softening of the A_g breathing mode is due to the spin-phonon coupling. Moreover, the O- and PD films differ significantly in the magnitude of $\Delta\omega(T)$ and in the temperature development, indicating a strong impact of the B-site ordering on the spin-phonon coupling, λ. The latter was determined from the linear approximation of $\Delta\omega(T)$ as a function of $M^2(T)/M^2_{max}$, taking the quarter of the absolute slope [18,23,49]. A linear relationship between $\Delta\omega(T)$ and $M^2(T)/M^2_{max}$ in Fig. 8(b), evidences a significantly stronger spin-phonon coupling for the O film, $\lambda_O \sim 2.1\,\mathrm{cm}^{-1}$, as compared to $\lambda_{PD} \sim 1.7\,\mathrm{cm}^{-1}$ for the PD film. Note, that the ratio $\lambda_{PD}/\lambda_O \sim 0.81$ is very close to the ratio between the squared saturation magnetization $(M_{s\text{-}PD}/M_{s\text{-}O})^2 \sim (0.9/0.98)^2 = 0.84$, obtained from the $M(H, 5\,\mathrm{K})$ loops (see Fig. 5) and also to the relative intensity ratio $I_{PD}/I_O = (I_{PD,xx}/I_{PD,xy})/(I_{O,xx}/I_{O,xy}) \sim 18/24.5 \sim 0.73$ of the breathing mode of both LCMO films in the parallel and the crossed scattering. Thus, the degree of

B-site ordering has not only a strong impact on the magnetic properties of the LCMO double perovskite system, but also on the phonon properties and the spin-phonon coupling strength, λ. Remarkably, the spin-phonon coupling serves as a characteristic parameter, which correlates all important features, i.e., structural/chemical ordering from XRD and EELS, phononic properties from T-dependent Raman measurements and magnetic properties from SQUID measurements.

Recently, the dependence of the spin-phonon coupling on the size of A cations was observed for A_2CoMnO$_6$ films ($A =$ Pr, Nd, Sm), grown on LAO(001) substrates [23]. The cation radius reduces for Pr to Sm and so does the spin-phonon coupling: $\lambda \sim 1.61\,\mathrm{cm}^{-1}$ (Pr), $\lambda \sim 1.20\,\mathrm{cm}^{-1}$ (Nd) and $\lambda \sim 1.16\,\mathrm{cm}^{-1}$ (Sm). This illustrates the influence of chemical pressure on the magnetic properties (T_C) and spin-phonon coupling as well. The underlying mechanism, probably, is the change of the orbital overlap and of the resulting FM superexchange due to decrease of the Co^{2+}-O^{2}-Mn^{4+} bond angle. Moreover, a very small $\lambda \sim 0.51\,\mathrm{cm}^{-1}$, obtained for bulk Pr$_2$CoMnO$_6$ [18], shows the importance of the epitaxy stress for the spin-phonon coupling in double perovskites. As for the LCMO/STO(100) films grown by PLD previously [16,17], one can, indeed, very roughly estimate the spin-phonon coupling constants from Fig. 5 (Ref. [16]) and Fig. 4(c) (Ref. [17]), getting $\lambda \approx 0.9$ and $1.1\,\mathrm{cm}^{-1}$, respectively.

We have performed a detailed analysis of spin-phonon coupling in LCMO films, epitaxially grown by MAD under the same conditions ($d \sim 100\,\mathrm{nm}$, temperature, oxygen partial pressure) on different substrates, i.e., STO(111), (LaAlO$_3$)$_{0.3}$(Sr$_2$TaAlO$_6$)$_{0.7}$(111) (LSAT), and LAO(111). The results are shown in Fig. 9 (see also Ref. [52]) and reveal that the strongest spin-phonon coupling constant, $\lambda = 2.1\,\mathrm{cm}^{-1}$, was obtained for the highly ordered LCMO O film on sapphire, which actuate a very small in-plane compressive
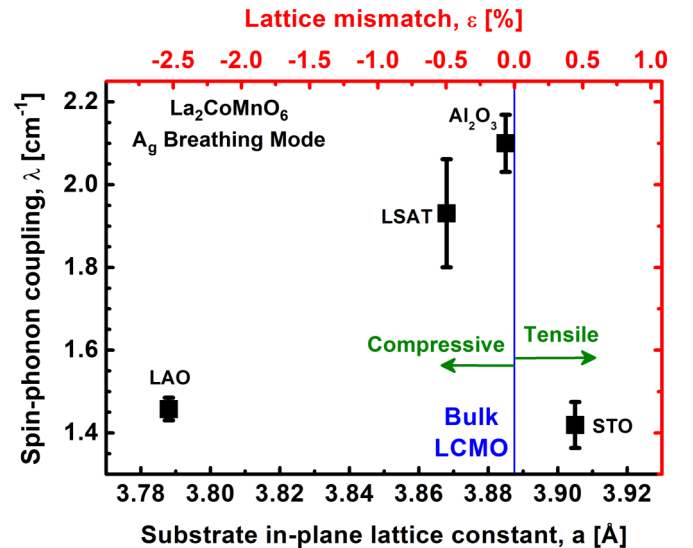

FIG. 9. A comparison of the spin-phonon coupling strength, λ, of the B-site ordered LCMO(111) thin films grown by MAD on different substrates, as a function of the in-plane lattice constant of the used substrates, a_{Sub}, or of the corresponding in-plane lattice mismatch, $\varepsilon = 100\% * (a_{Sub} - a_{LCMO})/a_{LCMO}$ with respect to the lattice constant of the bulk LCMO, $a_{LCMO} = 0.3887\,\text{Å}$.

strain. Note, that in the partially ordered LCMO PD film we obtained a smaller $\lambda = 1.7\,\text{cm}^{-1}$, indicating the impact of B-site ordering for the films with very similar and almost strain-free state. Moreover, one can see that a large lattice mismatch leads to a significantly smaller λ values, i.e., $\lambda \sim 1.5\,\text{cm}^{-1}$ for LAO(111) with large compressive stress (partially relaxed) and $\lambda \sim 1.4\,\text{cm}^{-1}$ for STO(111) with a tensile stress. Remarkably, a significantly larger spin-phonon coupling strength, $\lambda = 1.9\,\text{cm}^{-1}$, was obtained for the film grown on LSAT(111), which also actuates a relatively small in-plane compressive strain. Thus, one can conclude that the combination of the high degree of B-site ordering, small compressive epitaxy stress, and chemical pressure as well should result in a large spin-phonon coupling, which is a necessary attribute for a multiferroic material with high performance.

IV. CONCLUSION

Epitaxial double perovskite La_2CoMnO_6 thin films with monoclinic $P2_1/n$ structure and (021)/(201) out-of-plane orientation were grown on c-oriented Al_2O_3 (0001) substrates by the MAD technique. Through a combined characterization of structure, magnetism, and phonon properties a 98% degree of short-range B-site ordering was obtained suggesting a promising alternative substrate for the growth of double perovskite films. The B-site ordering was found to influence the phonon characteristics of the LCMO films as well as the temperature of structural phase transition to the rhombohedral $R\bar{3}$ structure. A strong impact of the B-site ordering on the strength of spin-phonon coupling was obtained.

[1] C. L. Bull, D. Gleeson, and K. S. Knight, J. Phys.: Condens. Matter **15**, 4927 (2003).

[2] A. J. Barón-González, C. Frontera, J. L. García-Muñoz, B. Rivas-Murias, and J. Blasco, J. Phys.: Condens. Matter **23**, 496003 (2011).

[3] P. Padhan and A. Gupta, in *Functional Metal Oxides*, edited by S. B. Ogale, T. V. Venkatesan, and M. G. Blamire (Wiley VCH Springer, Weinheim, Germany, 2013), pp. 51–88.

[4] M. P. Singh, K. D. Truong, and P. Fournier, Appl. Phys. Lett. **91**, 042504 (2007).

[5] M. P. Singh, S. Charpentier, K. D. Truong, and P. Fournier, Appl. Phys. Lett. **90**, 211915 (2007).

[6] R. I. Dass and J. B. Goodenough, Phys. Rev. B **67**, 014401 (2003).

[7] M. P. Singh, K. D. Truong, S. Jandl, and P. Forunier, J. Appl. Phys. **107**, 09D917 (2010).

[8] Y. Shimakawa, M. Azuma, and N. Ichikawa, Materials **4**, 153 (2011).

[9] S. Vasala and M. Karppinen, Prog. Solid State Chem. **43**, 1 (2015).

[10] R. Egoavil, S. Hühn, M. Jungbauer, N. Gauquelin, A. Béché G. Van Tendeloo, J. Verbeeck, and V. Moshnyaga, Nanoscale **7**, 9835 (2015).

[11] H. Z. Guo, A. Gupta, J. Zhang, M. Varela, and S. J. Pennycook, Appl. Phys. Lett. **91**, 202509 (2007).

[12] V. Shabadi, M. Major, P. Komissinskiy, M. Vafaee, A. Radetinac, M. Baghaie Yazdi, W. Donner, and L. Alff, J. Appl. Phys. **116**, 114901 (2014).

[13] S. Chakraverty, A. Ohtomo, D. Okuyama, M. Saito, M. Okude, R. Kumai, T. Arima, Y. Tokura, S. Tsukimoto, Y. Ikuhara, and M. Kawasaki, Phys. Rev. B **84**, 064436 (2011).

[14] S. Chakraverty, X. Z. Yu, M. Kawasaki, Y. Tokura, and H. Y. Hwang, Appl. Phys. Lett. **102**, 222406 (2013).

[15] K. Watarai, K. Yoshimatsu, K. Horiba, H. Kumigashira, O. Sakata, and A. Ohtomo, J. Phys.: Condens. Matter **28**, 436005 (2016).

[16] M. N. Iliev, M. V. Abrashev, A. P. Litvinchuk, V. G. Hadjiev, H. Guo, and A. Gupta, Phys. Rev. B **75**, 104118 (2007).

[17] K. D. Truong, J. Laverdière, M. P. Singh, S. Jandl, and P. Fournier, Phys. Rev. B **76**, 132413 (2007).

[18] D. Kumar, S. Kumar, and V. G. Sathe, Solid State Commun. **194**, 59 (2014).

[19] C. L. Bull and P. F. McMillan, J. Solid State Chem. **177**, 2323 (2004).

[20] D. Kumar and V. G. Sathe, Solid State Commun. **75**, 10 (2015).

[21] D. Kumar, S. Kumar, and V. G. Sathe, *Proceedings of the 59th DAE Solid State Physics Symposium 2014*, AIP Conf. Proc. No. 1665 (AIP, New York, 2015), p. 140030.

[22] C. Meyer, S. Hühn, M. Jungbauer, S. Merten, B. Damaschke, K. Samwer, and V. Moshnyaga, J. Raman Spectrosc. **48**, 46 (2017).

[23] C. Xie, L. Shi, J. Zhao, S. Zhou, Y. Li, and X. Yuan, J. Appl. Phys. **120**, 155302 (2016).

[24] K. D. Truong, M. P. Singh, S. Jandl, and P. Fournier, Phys. Rev. B **80**, 134424 (2009).

[25] M. N. Iliev, M. M. Gospodinov, M. P. Singh, J. Meen, K. D. Truong, P. Fournier, and S. Jandl, J. Appl. Phys. **106**, 023515 (2009).

[26] M. N. Iliev, H. Guo, and A. Gupta, Appl. Phys. Lett. **120**, 155302 (2007).

[27] J. E. Kleibeuker, E.-M. Choi, E. D. Jones, T.-M. Yu, B. Sala, B. A. MacLaren, D. Kepaptsoglou, D. Hernandez-Maldonado, Q. M. Ramasse, L. Jones, J. Barthel, I. Maclaren, and J. L. MacManus-Driscoll, NPG Asia Mater. **9**, e406 (2017).

[28] R. Galceran, L. López-Mir, B. Bozzo, J. Cisneros- Fernández, J. Santiso, L. Balcells, C. Frontera, and B. Martínez, Phys. Rev. B **93**, 144417 (2016).

[29] R. Galceran, C. Frontera, Ll. Balcells, J. Cisneros- Fernández, L. López-Mir, J. Roqueta, J. Santiso, N. Bagues, B. Bozzo, A. Pomar, F. Sandiumenge, and B. Martínez, Appl. Phys. Lett. **105**, 242401 (2014).

[30] L. López-Mir, R. Galceran, J. Herrero-Martín, B. Bozzo, J. Cisneros-Fernández, E.V. Pannunzio Miner, A. Pomar,

L. Balcells, B. Martínez, and C. Frontera, Phys. Rev. B **95**, 224434 (2017).

[31] L. López-Mir, C. Frontera, H. Aramberri, K. Bouzehouane, J. Cisneros-Fernández, B. Bozzo, L. Balcells, and B. Martínez, Sci. Rep. **8**, 861 (2018).

[32] V. Moshnyaga, I. Khoroshun, A. Sidorenko, P. Petrenko, A. Weidinger, M. Zeitler, B. Rauschenbach, R. Tidecks, and K. Samwer, Appl. Phys. Lett. **74**, 2842 (1999).

[33] V. Moshnyaga, A. Belenchuk, S. Hühn, C. Kalkert, M. Jungbauer, O. I. Lebedev, S. Merten, K.-Y. Choi, P. Lemmens, B. Damaschke, and K. Samwer, Phys. Rev. B **89**, 024420 (2014).

[34] M. Jungbauer, S. Hühn, R. Egoavil, H. Tan, J. Verbeeck, G. Van Tendeloo, and V. Moshnyaga, Appl. Phys. Lett. **105**, 251603 (2014).

[35] See Supplemental Material at http://link.aps.org/supplemental/10.1103/PhysRevB.98.134433 for structural details.

[36] K. Momma and F. Izumi, J. Appl. Crystallogr. **44**, 1272 (2011).

[37] M. K. Kim, J. Y. Moon, H. Y. Choi, S. H. Oh, N. Lee, and J. Choi, J. Phys.: Condens. Matter **27**, 426002 (2015).

[38] P. A. Stampe, M. Bullock, W. P. Tucker, and R. J. Kennedy, J. Phys. D: Appl. Phys. **32**, 1778 (1999).

[39] Z.-X. Mei, X.-L. Du, Z.-Q. Zeng, Y. Guo, J. Wang, J.-F. Jia, and Q.-K. Xue, Chin. Phys. Lett. **21**, 410 (2004).

[40] C. H. Jia, Y. H. Chen, G. H. Liu, X. L. Liu, S. Y. Yang, and Z. G. Wang, J. Phys. D: Appl. Phys. **42**, 015415 (2009).

[41] C. H. Jia, Y. H. Chen, G. H. Liu, X. L. Liu, S. Y. Yang, W. F. Zhang, and Z. G. Wang, Nanoscale Res. Lett. **8**, 23 (2013).

[42] D. P. Norton, Mater. Sci. Eng. R **43**, 139 (2004).

[43] A. J. Barón-González, C. Frontera, J. L. García, J. Roqueta, and J. Santiso, J. Phys. Conf. Ser. **200**, 092002 (2010).

[44] Y. Bai, Y. Xia, H. Li, L. Han, Z. Wang, X. Wu, S. Lv, X. Liu, and J. Meng, J. Phys. Chem. C **116**, 16841 (2012).

[45] X. L. Wang, M. James, J. Horvat, and S. X. Dou, Supercond. Sci. Technol. **15**, 427 (2002).

[46] See Supplemental Material at http://link.aps.org/supplemental/10.1103/PhysRevB.98.134433 for anharmonic model.

[47] M. N. Iliev, H. Guo, and A. Gupta, Appl. Phys. Lett. **90**, 151914 (2007).

[48] Y. Chen, B. Peng, and B. Wang, J. Phys. Chem. C **111**, 5855 (2007).

[49] E. Granado, A. García, J. A. Sanjurjo, C. Rettori, I. Torriani, F. Prado, R. D. Sánchez, A. Caneiro, and S. B. Oseroff, Phys. Rev. B **60**, 11879 (1999).

[50] J. Laverdière, S. Jandl, A. A. Mukhin, V. Yu. Ivanov, V. G. Ivanov, and M. N. Iliev, Phys. Rev. B **73**, 214301 (2006).

[51] P. K. Pandey, R. J. Choudhary, D. K. Mishra, V. G. Sathe, and D. M. Phase, Appl. Phys. Lett. **102**, 142401 (2013).

[52] C. MeyerOrdnung-/Unordnungsphänomene in korrelierten Perowskitschichten anhand von fort-geschrittener Raman-Spektroskopie, Ph.D. Dissertation, Georg-August-Universität, Göttingen, 2018.